Electronic Supplementary Material (ESI) for Energy & Environmental Science.
This journal is © The Royal Society of Chemistry 2022

Supporting Information for

A Sobering Examination of the Feasibility of Aqueous Aluminum Electrolyte

Glenn R. Pastel,‡[a] Ying Chen,‡[b] Travis P. Pollard,‡[a] Marshall A. Schroeder,[a] Mark E. Bowden,[b] Allen Zheng,[c] Nathan T. Hahn,[d] Lin Ma,[a] Vijayakumar Murugesan,[b] Janet Ho,[a] Mounesha Garaga,[c] Oleg Borodin,[a] Karl Mueller,[b] Steven Greenbaum,[c] and Kang Xu*[a]

[a] Battery Sciences Branch, U.S. Army Research Laboratory, Adelphi, Maryland 20783, United States
[b] The Joint Center for Energy Storage Research (JCESR), Pacific Northwest National Laboratory, Richland, WA 99354, USA.
[c] Department of Physics & Astronomy, Hunter College of the City University of New York, New York, NY 10065 USA.
[d] The Joint Center for Energy Storage Research (JCESR), Sandia National Laboratories, Albuquerque, NM 87123, USA.

* Corresponding Author

MATERIALS AND METHODS

Electrolyte Preparation. Aluminum trifluoromethanesulfonate ($Al(CF_3SO_3)_3$, 99%, SynQuest Laboratories, Inc., USA and 99%, Alfa Aesar, USA) was used as-received or after drying by various methods. The water content of the salt was determined by Karl Fisher titration measurements (728/831 KF Coulometer, Metrohm, Germany) in acetonitrile or dimethyloxyethane (H_2O content < 50 ppm) after drying with 3 Å molecular sieves or phosphorus pentoxide (P_4O_{10}) (Sigma Aldrich, USA). Aqueous electrolyte solutions were prepared by dissolving an appropriate amount of aluminum triflate in ultrapure water (>18 MΩ.cm, Millipore, USA). Discoloration and precipitates were observed in solutions with aluminum triflate sourced from Alfa Aesar. The composition of the aqueous solutions are described in molality (m) with consideration for the hydration content of the salt.

Deep eutectic solvent for pre-treating aluminum electrodes was prepared by slowly mixing 1-ethyl-3-methylimidazolium chloride ([EMIM]Cl; 98+%, TCI America, USA) with anhydrous aluminum chloride ($AlCl_3$ 99.99%, Sigma Aldrich, USA) in a 1:1.3 mole ratio. 0.5M hydrochloric acid was prepared by diluting concentrated acid (Sigma Aldrich, USA) with Millipore water. Phosphoric acid (H_3PO_4, 60%) was used without additional preparation.

Electrode preparation. Aluminum, carbon, and other electrodes were prepared by wet polishing with up to 1200 grit sandpaper followed by sonicating in methanol and ultrapure water. The active area of the working electrode never exceeded half the active area of the counter electrode. Calibrated Ag/AgCl reference electrodes were used in beaker and Swagelok cell configurations while a Pt wire pseudo-reference was used for optical cell measurements.

After each experiment, platinum wire was etched in piranha solution (3:1 sulfuric acid to 30% hydrogen peroxide, Sigma Aldrich, USA) for at least five minutes before washing thoroughly with ultrapure water. The active surface area of the Pt wire was approximated from the length immersed in electrolyte. Although the length of wire immersed in electrolyte remained relatively constant across all measurements, a ±10% error bar is expected for the active surface area.

In scans investigating the impact of various pre-treatment procedures on electrochemical stability, aluminum foil with 100 micron thickness (Alfa Aesar, USA) was prepared accordingly and wrapped over an aluminum rod.

Electrochemical Measurements. Beaker, Swagelok, and custom optical cell configurations for various three electrode measurements were performed on a Biologic SP-150 or PARSTAT MC Potentiostat. In beaker cell experiments, electrodes were spaced 100 μm apart and wrapped in place with Teflon tape, without a rigid separator layer, and at least 400 μL of electrolyte. In Swagelok cell experiments, the working and counter electrode were separated by two glass fiber separator layers (Whatman QMA, USA) and soaked in at least 200 μL of electrolyte. The reference electrode was carefully inserted between the separator layers, in close proximity to the working electrode. In custom-designed optical cell, a single separator layer ensured at least 150 μm of spacing between electrodes with approximately 100 μL of electrolyte. Fresh electrolyte was prepared for each experiment.

Solution-state NMR. ^{1}H, ^{17}O, ^{19}F, ^{27}Al solution-state NMR measurements of $Al(OTf)_3$ in D_2O solutions were performed on a Varian DDRS 17.6 T spectrometer using a broad-band (BBO) probe with ^{1}H, ^{17}O, ^{19}F, and ^{27}Al Larmor frequencies of 748.1, 101.4, 703.7, and 194.9 MHz, respectively. The 90˚ pulse widths were 20 µs for ^{1}H, 16 µs for ^{17}O, 22 µs for ^{19}F, and 15 µs for ^{27}Al. For obtaining quantitative integration ratios between OTf, bridging oxygen and free water, ^{17}O spectra were collected by setting the carrier frequency halfway between the OTf and free water signals and using a small tip angle of 15° with a recycling delay of 0.2 s and 32,000 transients at each temperature. The “NOESY” pulse sequence within VnmrJ was used to measure ^{1}H-^{1}H EXSY with a spectral width of 10,000 Hz, 40 increments in the indirect dimension, 16 scans per increment, and a range of mixing times (10 ms, 20 ms, 30 ms, and 50 ms). A zero-quantum, (ZQ) filter was used for mixing times greater than 30 ms. Chemical shifts for ^{1}H, ^{17}O, ^{19}F, ^{27}Al spectra were referenced to 10 mM DSS in D_2O (0 ppm), pure D_2O (0 ppm), CF_3CH_2OH (-76.55 ppm), and 1 M $AlCl_3$ in D_2O (0 ppm), respectively.

Solid-state MAS NMR. Single-pulse ^{1}H, ^{17}O, and ^{27}Al MAS NMR experiments of $Al(OTf)_3$ in H_2O solutions were performed on a Varian DDRS 20.0 T (with a ^{27}Al Larmor frequency of 221.41 MHz) NMR spectrometer using our home-built NMR probe with 5 mm sealable *WHiMS* rotors[35] (to prevent liquid leakage) with a spinning speed of 5 kHz.

SCXRD. Single crystals were obtained by slowly lowering the temperature of a 5 mm NMR tube filled with statured solutions (3.3 m $Al(OTf)_3$ in D_2O or 3.6 m $Al(OTf)_3$ in H_2O) inside the 17.6 T magnet from 50 °C to -10 °C in about 6 hours and staying at -10 °C for overnight. The liquids were removed immediately from the NMR tube afterwards and the clear crystals were stored inside the tube for SCXRD measurements. Single crystals could also be obtained by slowly evaporating water under N_2 environment for 24 hours.

Low temperature data was collected using a Bruker Quest diffractometer equipped with a microfocus Mo Kα x-ray source. A crystal was mounted on a nylon loop under a cryostream at 100 K, and φ and ω scans collected to cover 49,346 reflections. Multi-scan absorption corrections were applied to the measured intensities and the structure solved using SHELXS before refinement using OLEX2 v1.5. Non-hydrogen atoms were refined with anisotropic displacement parameters; hydrogen atoms were refined isotropically in positions restrained by their chemical environment. Further details and references can be found in the CIF available from the CCDC and supplemental information.

Pulse Field Gradient Nuclear Magnetic Resonance Spectroscopy. ^{1}H, ^{19}F, and ^{27}Al diffusion coefficients of aqueous Al electrolytes were measured on a 300 MHz NMR spectrometer operating at a magnetic field of 7T (^{1}H, ^{19}F, and ^{27}Al Larmor frequencies of 300, 284.4 and 78.5 MHz, respectively) equipped with DOTY Z-spec pulsed field gradient (PFG) NMR probe. The signal was accumulated over 16-256 transients with 2-10 s recycling delay. The diffusion coefficients were measured at 25 °C by using spinecho pulse sequence. The gradient strength was varied in the range of 10–900 G/cm for 16 increments.

The diffusion time (Δ) and the diffusion pulse length (δ) were set to 6-20 ms and 1.2-5 ms, respectively. The diffusion coefficients were calculated by using Stejskal-Tanner equation.

pH and Conductivity. Measurements were performed with either Mettler Toledo FiveEasy pH/mV & Conductivity meters. Calibration with 1.68, 4.00, 7.00, and 10.00 pH solutions was performed daily with additional single measurements checks between each measurement. Additional information regarding the use and maintenance of pH and conductivity meters is available through the Mettler Toledo online library.

Thermogravimetric Analysis and Mass Spectroscopy. Measurements were performed with a TA Instruments TGA5500 with a Discovery quadrupole mass spectrometer. Samples were sealed in aluminum pans in the glovebox before transferring to the TGA. A ramp protocol from ambient temperatures up to 400 °C at 1 °C min^{-1} was used. Gasses measured include: H, He, H_2O, N_2/CO, O, Ar, and CO_2.

Differential Scanning Calorimetry. Measurements were performed with a TA Instruments Discovery 250 with a Liquid Nitrogen Cooling Unit. Forward and reverse scans were performed between ambient temperatures and up to around 260 °C at a 10 °C min^{-1} scan rate. Samples were sealed in aluminum pans in the glovebox before transferring to the DSC.

Raman Spectroscopy. Raman vibrational spectra were collected with a Renishaw inVia Raman microscope using a 785 nm^{-1} laser as the exciting source and a 20x optical objective. Spectra were typically collected using 1% laser power, 10 to 30 sec exposure time, and one accumulation.

X-ray Diffraction. Spectra were collected with a Rigaku Miniflex XRD system between 3 and 90° at a 10° min^{-1} scan rate.

Dielectric Relaxation Spectroscopy Measurements. DRS measurements were performed in glass vials using a dielectric probe kit (Keysight N1501A) and vector network analyzer (Keysight P9375A), which were calibrated using air, acetonitrile, and water. The complex permittivity was measured from 0.5 to 26.5 GHz and the experimental data was fit using two Debye relaxation processes for solvent and salt components at or below 1.0 m. Solutions at higher concentrations were fit with one Debye and Cole-Cole function to account for feature broadening. Solutions with the highest ionic conductivity (0.5, 1.0, and 2.0 m) showed significant artifacts in the ε' data below 0.8 GHz and this region was excluded from the fitting. Extrapolation of the fitted spectra to zero frequency yields the dielectric constant of each solution.

Computational Studies – Prediction of Raman active modes and hydrogen evolution potentials. All calculations related to the Raman spectra were performed using Avogadro[3] for set up of molecular clusters, Atomic Simulation Environment[4] for preparation of input, and Gaussian 16 rev C.01[5] for all density functional theory calculations. Initially structures were taken from previous work[6] and the Zn^{2+} replaced with Al^{3+}, where we had difficulties reproducing sensible frequencies for symmetric ν(SO_3) using implicit solvation (PCM and SMD, acetone and water) with the M05-2X functional and double and triple-zeta flavors of the Pople basis sets. We then sampled ~30 different functionals in gas phase for the bare triflate anion using Dunning's aug-cc-pVTZ basis set. Given the simple nature of these calculations (gas phase + harmonic approximation for frequencies), we focused on functionals that were either very close to (scaling factor ~1) or somewhat overestimated (scaling factor <1) symmetric ν(SO_3) ***and*** ν(CF_3) frequencies.[7] Several functionals met this criteria, including M05-2X, BMK, LC-BLYP, LC-wHPBE, M06-2X, and SOGGA11X – all hybrid functionals including some portion of exact exchange from Hartree-Fock. We then found 6-31+G(2d) to better reproduce the aug-cc-pVTZ frequencies for each functional than aug-cc-pVDZ; this reduction in basis set size is necessary for the cluster calculations. This basis set was augmented with diffuse (+) and polarization functions (2p) for the hydrogens in water. All data in Figure S9 uses LC-BLYP/6-31++G(2d,2p).

Hydrogen evolution onset potentials were computed at the PCM(acetone, acetonitrile, water)/M05-2X/6-311++G(3df,3pd) level of theory from the conversion of $[Al(H_2O)_6]^{3+}$ to $[Al(OH)(H_2O)_5]^{2+}$ and $1/2H_2$ according to,

$$E^{red} = -\frac{\Delta G^{298}(A^-) + 0.5 * \Delta G^{298}(H_2) - \Delta G^{298}(A)}{nF} - 4.662$$

where, n is the number of electrons, F is Faraday's constant, ΔG's are free energies from density functional theory for the reduced species (A^-), H_2, and the not reduced species (A). A 4.662 V shift adjusts the result to the Ag/AgCl scale (4.44 V standard hydrogen electrode absolute potential + 0.222 V Ag/AgCl standard reduction potential).

Born-Oppenheimer Molecular Dynamics. Packmol[8] was used to generate four unique configurations for simulations using a random seed at a concentration of 3.6 molal, corresponding to a water:Al ratio of 16:1. Four initial configurations were generated by packing $4*[Al(H_2O)_6]^{3+}$, $12*[OTf]^-$, and 40 free water monomers. The initial packing density was 1.6 g/mL using a box length of ~14.68 Å.

Unfortunately, random packing results in a highly heterogeneous second solvation shell with the anions tending to be clumped up together, resulting in large voids between the CF_3 groups that would not relax on BOMD timescales. In an effort to improve the quality of the initial structure, molecular dynamics was performed first with the OPLSAA force field using SPC water[9], OPLS-AA ionic liquid OTf (charges scaled by 0.8)[10], and Al^{3+} parameters (charge scaled by 0.8) from Faro, Thim, and Skaf[11]. All force field calculations were performed using Tinker 8.1.0[12]. Initially we did use full scale charges but it was found that the scaled charges better reproduced the experimental density and did not require scaling the $Al\text{-}O_{triflate}$ σ_{ij} by ~13% to exclude all triflate from the first solvation shell. About 10 ns (NPT 330 K, 1 atm) and 24 ns (NVT 330 K) were run using integer charges and the same cutoffs and thermostat/barostat as described below. The density converged to ~1.59 g/mL, very close to that of experiment. Initial testing with CP2K revealed there was a sizeable barrier for the initial dissociation reaction that produces solvated H_3O^+, so these configurations were used as inputs for calculations prepared at a higher temperature. Born-Oppenheimer molecular dynamics runs were planned to use a target temperature of 800 K to overcome this barrier within a ~40 ps time window. These configurations were brought to new target conditions of 373 K at 1 atm over 4 ns using a 1 fs time step and the Bussi thermostat and Berendsen barostat[13, 14]. At both temperatures, Coulomb real-space and vdW cutoffs were limited to 7.0 Å, using a particle mesh Ewald grid of 18x18x18 with spline order 5, and long range vdW corrections. Densities converged to ~1.54 g/mL within the 1st nanosecond and we scaled the density by a factor of 0.9 to calculate the average box size (1.386 g/mL, ~15.402 Å per side). Rescaling the final snapshots from each trajectory to the new box size, a further 24 ns of dynamics at 373 K with a 2 fs time step were performed in the NVT ensemble with the Bussi velocity rescaling thermostat[13]. The final configuration from each trajectory is taken as a starting point for BOMD.

All Born-Oppenheimer molecular dynamics (BOMD) calculations were carried out with CP2K v8.2[15] at the revPBE-D3BJ level of theory with DZVP-MOLOPT-SR-GTH basis set and PBE-GTH pseudopotentials[16-23]. Geometries were taken as is from the classical trajectories above and relaxed to their DFT bond lengths over 1.0 ps at 50 K using a 0.5 fs timestep (further details in Supplementary Table S5). Subsequent thermalization, equilibration, and production steps are highlighted in this table as well – all calculations are in the NVT ensemble with cubic symmetry and lattice parameter a = 15.402 Å. DCD binary files with the coordinates from the 30 ps MD-6 stage and associated restart files are attached in a tarball as additional supporting information. The restart file from the final snapshots and associated wave function file can be used to directly continue the calculations. An Atomic Simulation Environment[4] (we used version 3.22.0) script is included as well to convert the binary DCD file to XMOL/xyz format. A 0readme.md file gives additional details. Visuals were prepared with Jmol[24] and rendered in POVRay 3.7. The TRAVIS analyser was used to autodetect bonds and wrap molecules into the box rather than just atoms to clean up the visuals slightly.[25]

FIGURES

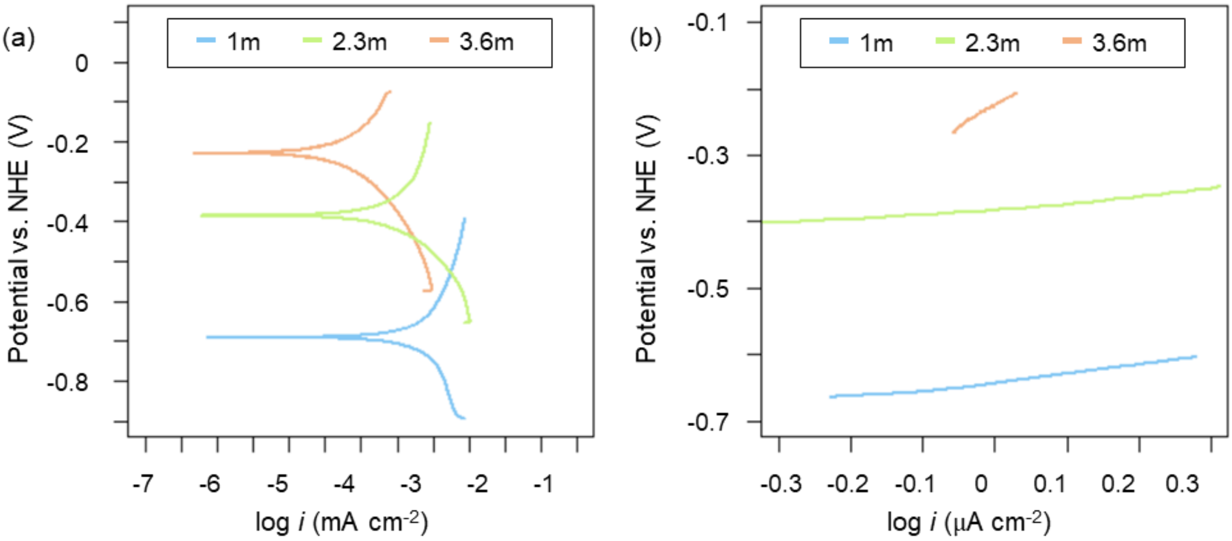

Figure S1. Tafel and linear polarization resistance results from 1.0 m, 2.3 m, and 3.6 m $Al(OTf)_3$-H_2O solutions with an aluminum working electrode, Ag/AgCl reference electrode, and glassy carbon counter electrode.

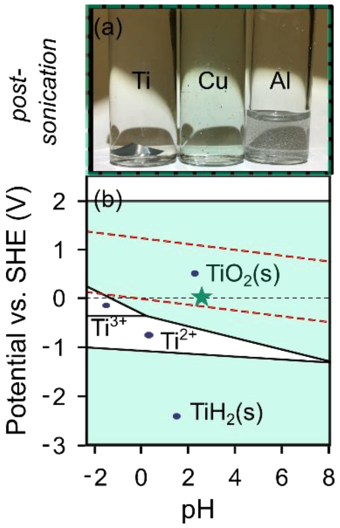

Figure S2. (a) Images of Ti, Cu, and Al metal in 1.0 m $Al(OTf)_3$-H_2O solution after intermittently sonicating for one week. The titanium metal remained completely intact, in stark contrast to copper and aluminum. However, the Pourbaix diagram for titanium (b) indicates the metal will not be stable under reductive potentials without additional passivation or kinetic hindrance.

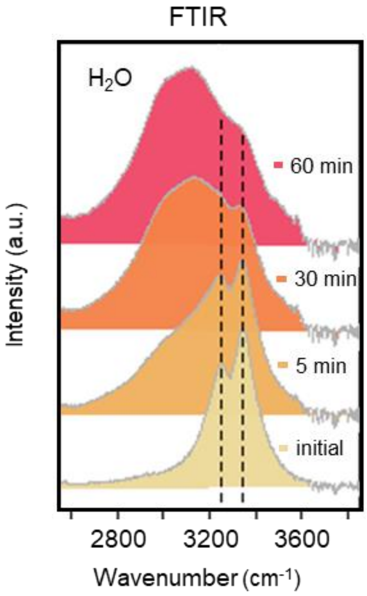

Figure S3. Fourier transform infrared spectroscopy (FTIR) of aluminum triflate before and after exposing to ambient moisture (~35% RH) with a focus on the O-H stretching region.

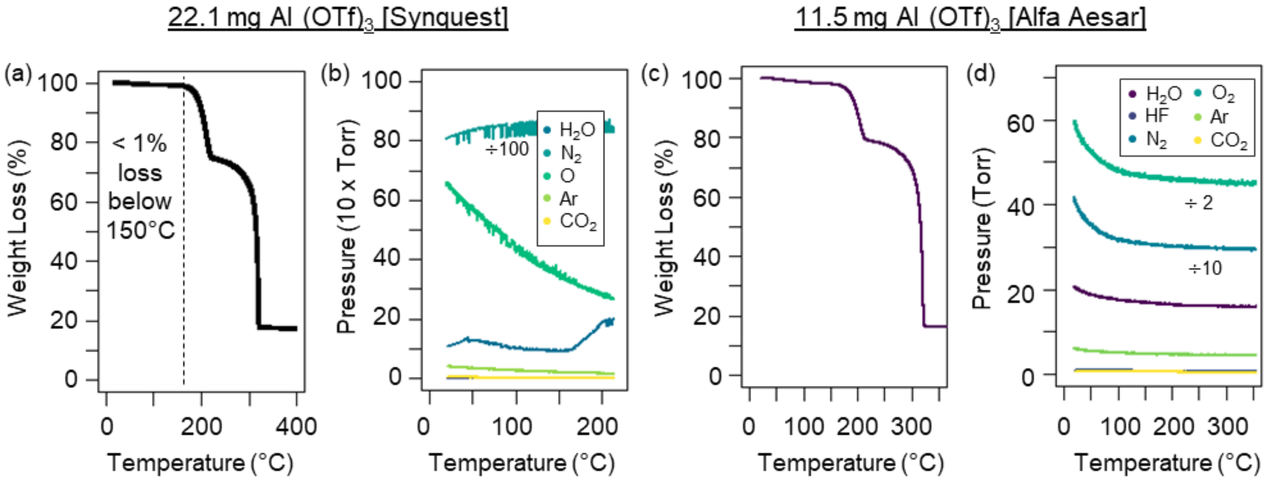

Figure S4. (a, c) Thermogravimetric analysis of 22.1 mg and 11.5 mg of Al(OTf)₃ sourced from SynQuest Laboratories, Inc. and Alfa Aesar, respectively. A ramp protocol between 20 and 400 °C at 1 °C min^{-1} was performed with (b, d) *in operando* mass spectrometry of the evolved gasses. An insignificant amount of weight loss (< 1 wt%) occurs in both samples below 150 °C.

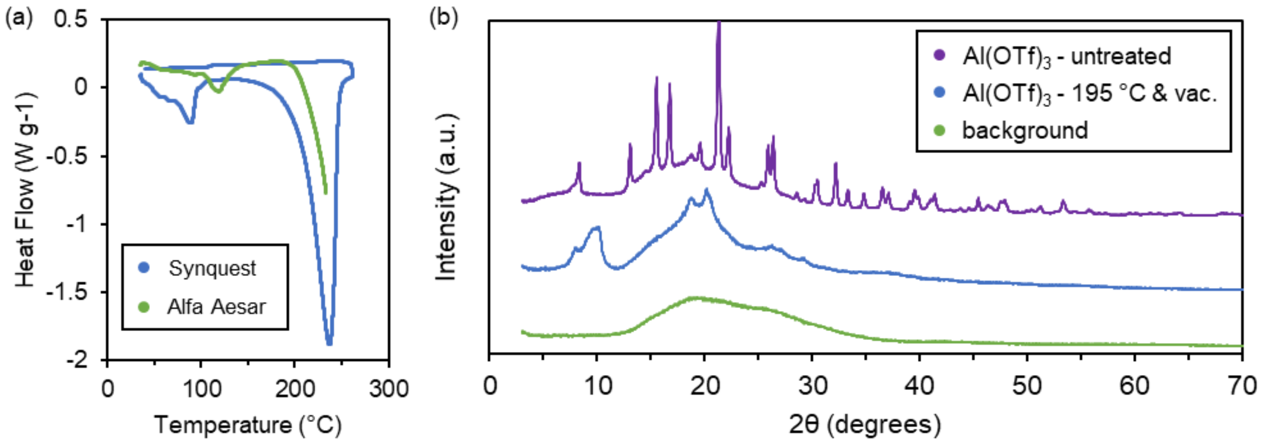

Figure S5. (a) Differential scanning calorimetry of 4.0 mg $Al(OTf)_3$ from Synquest and 2.7 mg $Al(OTf)_3$ from Alfa Aesar ramped up to 261 and 233 °C, respectively, at 10 °C min^{-1}. Endothermic melting or decomposition reactions are irreversible, without an exothermic recrystallization process in the reverse scan. Post-mortem analysis indicates the Alfa Aesar material is still a powder after incomplete melting, while the Synquest material is an agglomerated, melted solid. (b) X-ray diffraction spectra indicates a change in composition after heating $Al(OTf)_3$ (Alfa Aesar, USA) to 195 °C under vacuum for 1 hour. The amount of amorphous alumina in the heat treated product is substantial and indicates that $Al(OTf)_3$ cannot be thermally dehydrated.

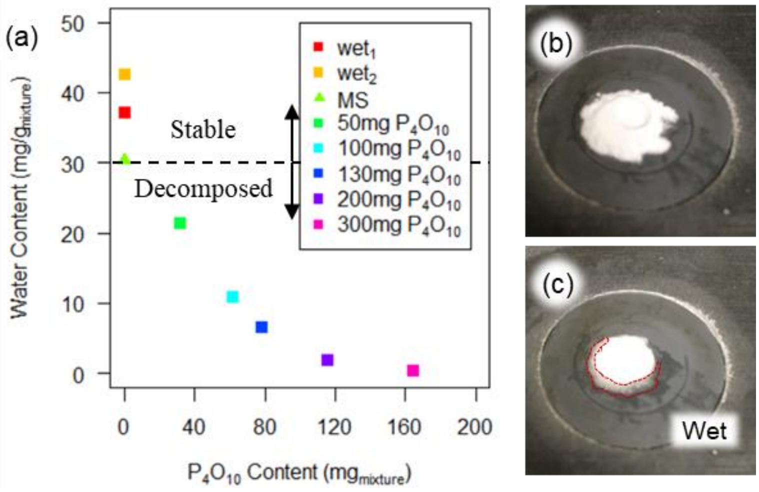

Figure S6. (a) Water content of 523.7 mg $Al(OTf)_3$ (SynQuest Laboratories, Inc.) in 1.00 g of dry acetonitrile (24.77 ppm H_2O) measured by Karl Fisher titration. Adsorption and chemical drying agents were tested to reduce the water content. Hygroscopic aluminum triflate as a dry powder (b) immediately after exposing to ambient humidity and (c) wet after exposure for 1 hour.

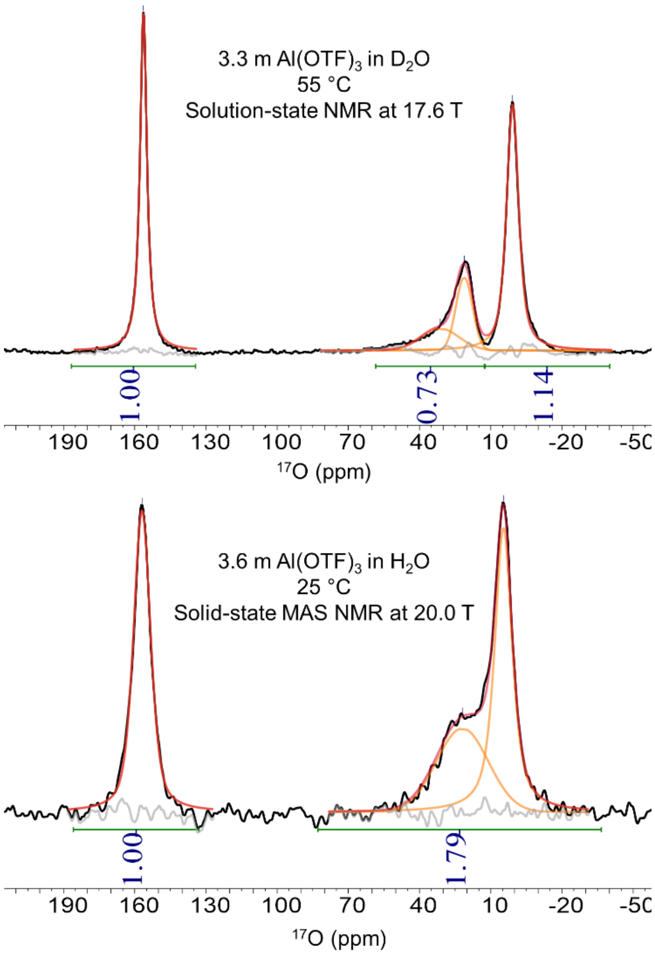

Figure S7. Deconvolution of the ^{17}O NMR spectra shows the molar ratio between the bound and free water. The ratio between the total molar content of solvent to OTf can also be quantitatively estimated by comparing the respective signals.

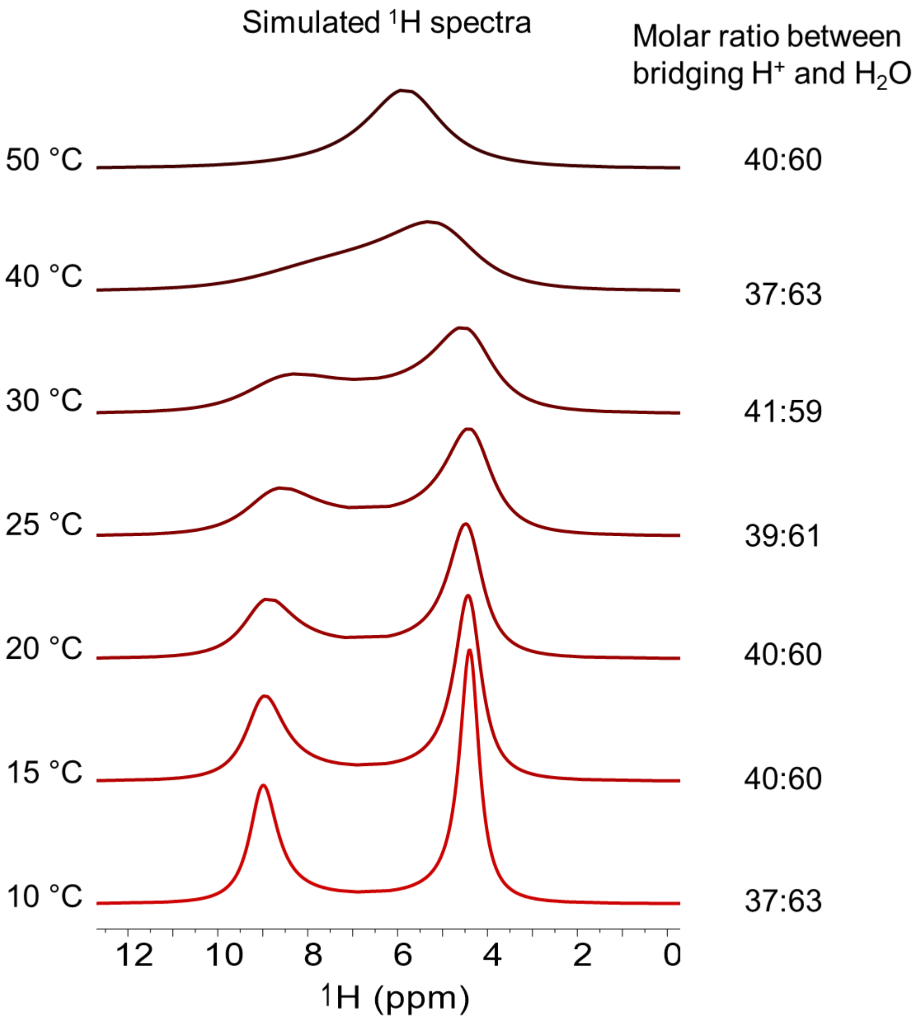

Figure S8. Simulated ^{1}H spectra using the 'dnmr' lineshape analysis package in Topspin 3.6. The exchange rates and molar ratio between the two states can be obtained by fitting the experimental spectra at varying temperatures.

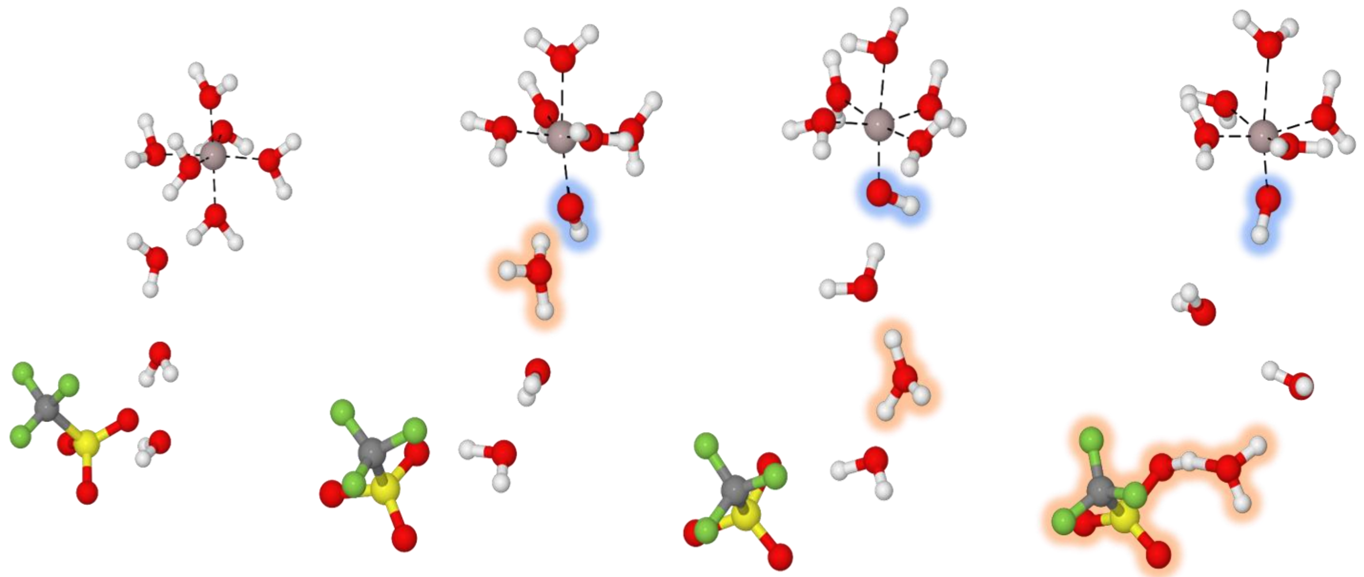

Figure S9. Snapshot from one of the Born Oppenheimer molecular dynamics simulation trajectories highlighting the Grotthuss mechanism for forming H_3O-OTf ion pairs. A blue glow denotes Al^{3+}-bound OH and orange denotes proton related species (e.g., hydronium, Zundel cation, or H_3O-OTf ion pairing).

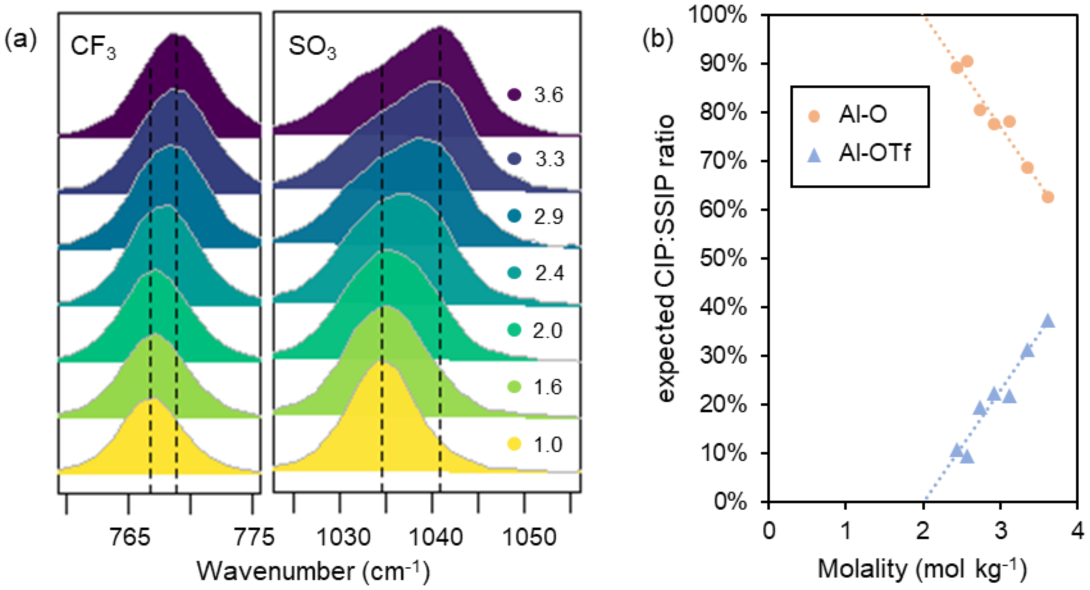

Figure S10. (a) Raman spectra of the CF_3 and SO_3 vibrational bands for $Al(OTf)_3$-H_2O solutions around 768 and 1034 cm^{-1}, respectively, with 3.61 m (top) to 1.38 m (bottom) at 20 °C. (b) Previous interpretations of the blueshift of the SO_3 vibrational bands for $Al(OTf)_3$-H_2O solutions from 1034 to 1041 cm^{-1} related to approximately 40% Al-OTf contact ion pair formation near the room temperature solubility limit. Direct correlation of this blueshift to CIP formation is curbed due to observation of a similar trend for H-OTf dilutions, with comparable mole ratios of free OTf to free water. A linear fit of the change in 1034 and 1041 cm^{-1} signal ratio, assuming two symmetric Gaussians, has a high R squared values of 0.9388.

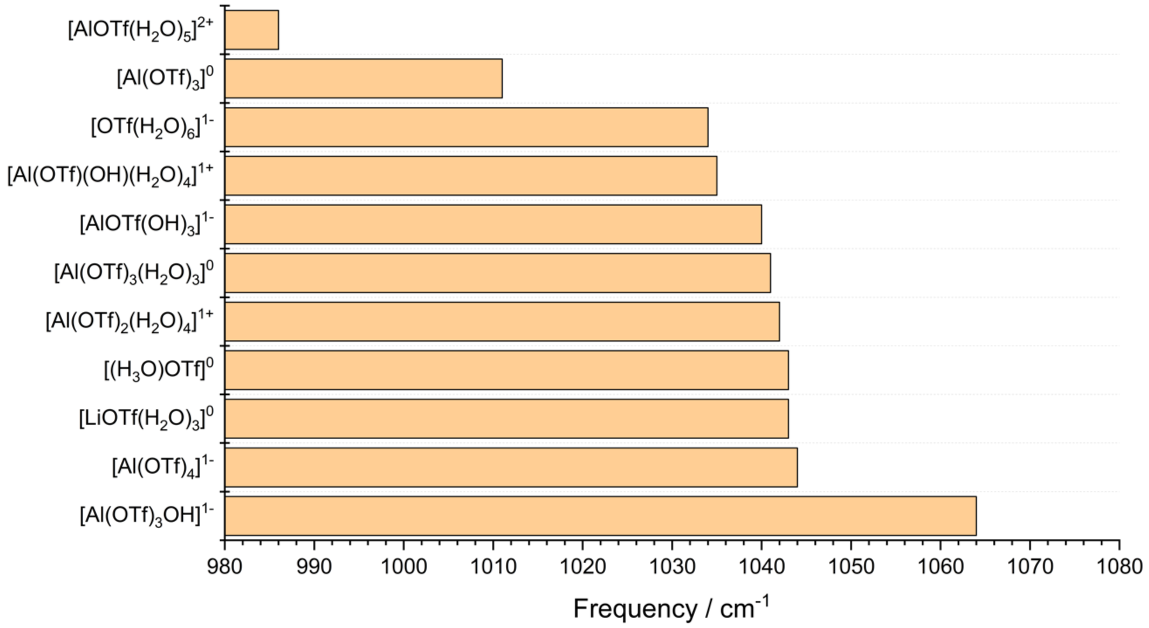

Figure S11. Scaled Raman frequencies for the symmetric SO_3 stretching mode from LC-BLYP/6-31++G(2d,2p). Sorted in order of increasing frequency from top to bottom. $[OTf(H_2O)_6]^{1-}$ is scaled by 0.954814 to exactly 1034 cm^{-1} and $[LiOTf(H_2O)_3]^0$ is scaled by 0.962793 to exactly 1043 cm^{-1}. All Al^{3+} or H_3O^+ containing clusters are scaled by 0.962793 as well. In terms of raw frequencies, every method considered gave a higher frequency for $[OTf(H_2O)_6]^{1-}$ than $[LiOTf(H_2O)_3]^0$ which is the reason for the different scaling factors. The names in the figure reflect the first shell compositions. In several of these structures, first shell waters will hydrogen bond to the first shell triflate or hydroxide ions. This results in a distorted octahedral geometry and generally greatly redshifts the SO_3 mode. In those cases, some additional second shell waters (typically 2-3) would be added to break up those interactions, restoring a more idealized octahedral geometry and usually blueshifting the SO_3 mode. For the sake of clarity, these waters are not accounted for or referenced in the figure. The $[(H_3O)OTf]^0$ shell includes 4 additional waters. While there are a number of Al-OTf contact ion pair solvate structures with $v(SO_3)$ bands in the right position (1040-1044 cm^{-1}), all of them are eliminated by the absence of evidence of CIP formation between Al^{3+} and OTf^- from NMR; the Lewis acid-base adducts of $Al(OH)_3$ + OTf^- and $Al(OTf)_3$ + OTf^- doubly so since no resonances are observed consistent with a tetrahedral solvation shell. Only H_3O-OTf remains.

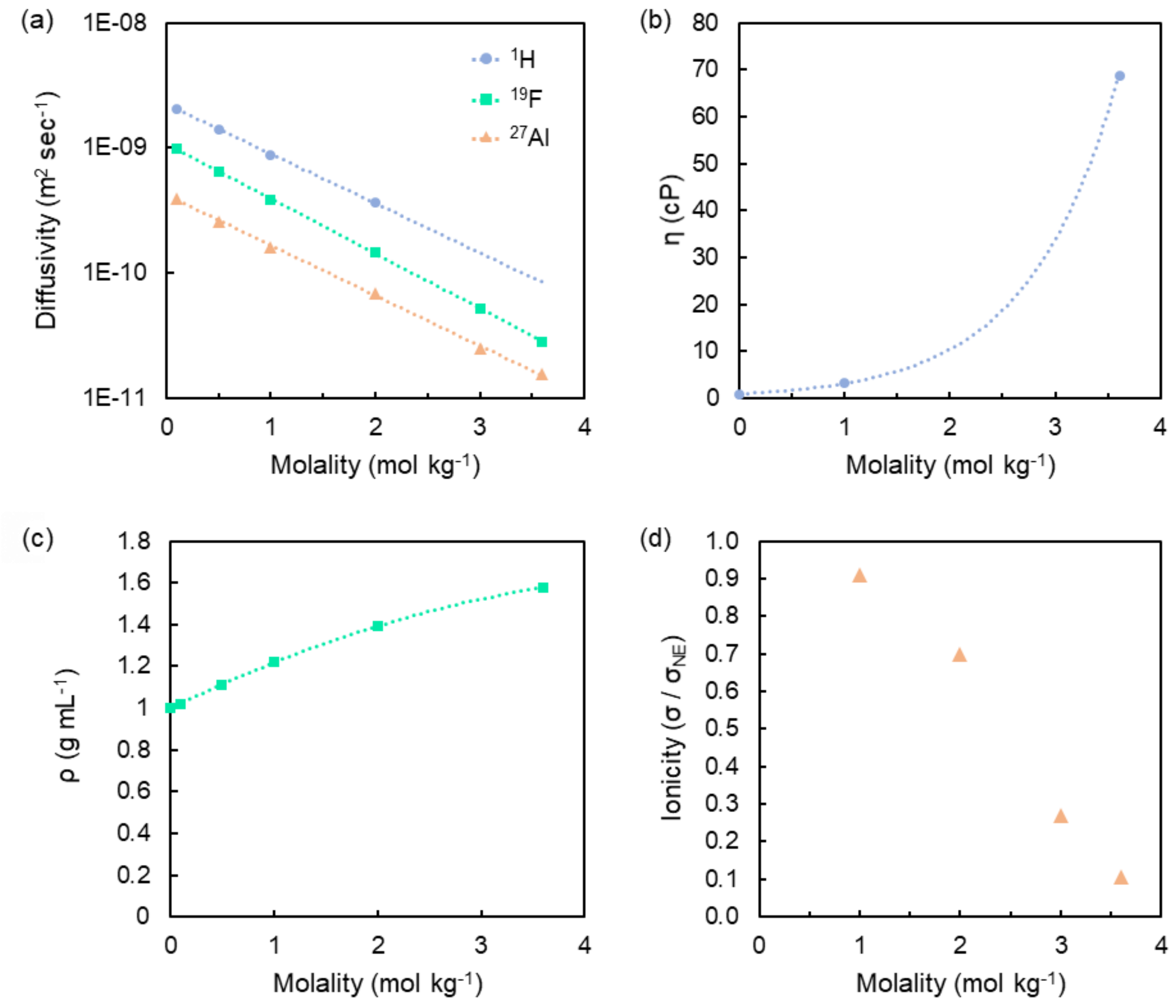

Figure S12. (a) Diffusion coefficients of ^{1}H, ^{19}F, and ^{27}Al as measured by PFG-NMR at six $Al(OTf)_3$-H_2O concentrations. The dotted lines are linear regressions for the points, with Pearson's correlation coefficients $R > 0.995$. (b) Viscosity of pure water, 1.0 m, and 3.61 m solutions fitted to an exponential regression line with a Pearson's correlation coefficient $R = 0.9999$. (c) Density at six $Al(OTf)_3$-H_2O concentrations fitted to a polynomial with a Pearson's correlation coefficient $R = 0.9998$. (d) Ionicity of the $Al(OTf)_3$-H_2O solutions benchmarked against the Nernst-Einstein conductivity as predicted with charge neutral Al^{0+} species. All measurements were performed at room temperature, approximately 20.7 °C.

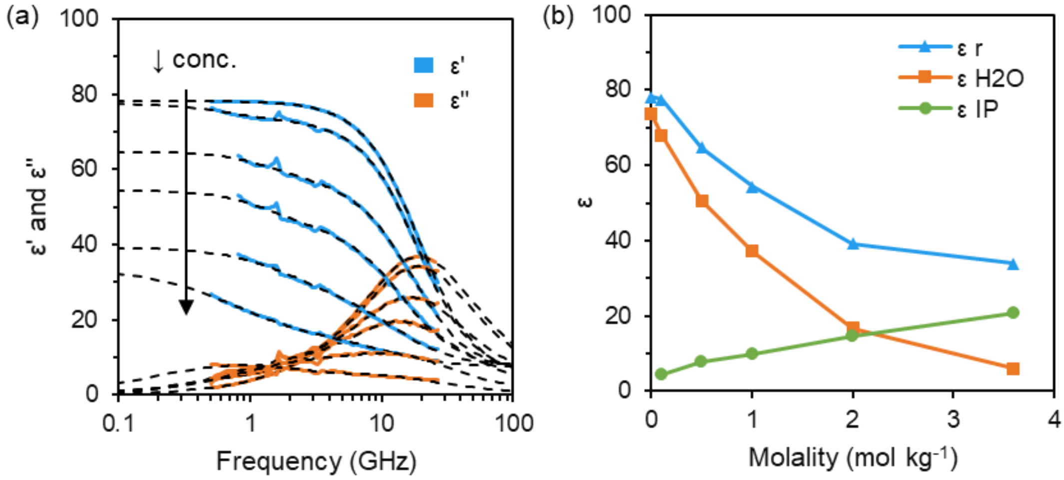

Figure S13. (a) Complex permittivity spectra measured by dielectric relaxation spectroscopy of six Al(OTf)$_3$-H$_2$O solutions with concentrations of 0, 0.1, 0.5, 1.0, 2.0, and 3.6 m. Permittivity (ε’, blue solid lines) and dielectric loss (ε”, orange solid lines) are fit to two Debye functions at lower concentrations (≤ 1.0 m) and to one Debye and one Cole-Cole function at higher concentrations (≥ 2 m). The fit spectra are indicated by dashed black lines, which are extrapolated beyond the measured range. (b) The total dielectric constant (ε_r) and permittivity contributions from unbound water (ε_{H2O}) and ion pairs (ε_{IP}) based on the spectral deconvolution. The binding of water by Al^{3+} leads to a significant drop in ε_r as salt concentration is increased. The species giving rise to the ε_{IP} contribution are most likely solvent-shared ion pairs (SIPs) in which the OTf$^-$ exhibits significant residence time in the 2nd solvation shell of Al^{3+} due to strong electrostatic attraction.

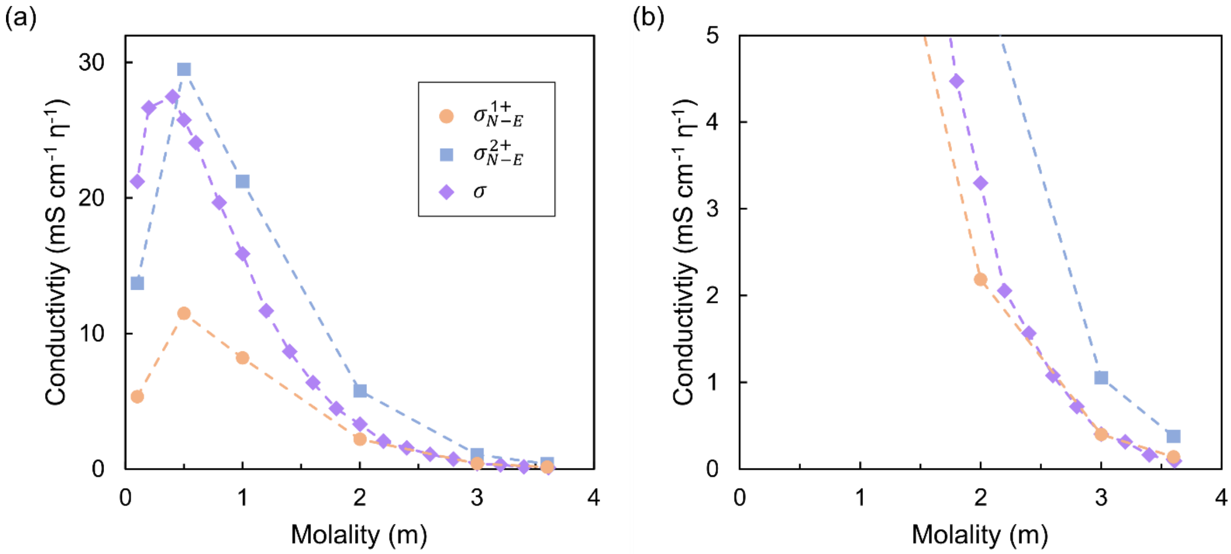

Figure S14. (a, b) The ionic conductivity of Al(OTf)$_3$-H$_2$O solutions predicted from PFG-NMR diffusivity measurements with the measured conductivity (purple diamond); Al with a +2 oxidation state, only 2/3 of the OTf$^-$ anions contributing to the Nernst-Einstein conductivity due to HOTf formation with 1/3 of the triflate anions by salt stoichiometry (blue triangle); and Al with a +1 oxidation state with only 1/3 of the OTf$^-$ anions contributing to the Nernst-Einstein conductivity due to HOTf formation with 2/3 of the triflate anions by salt stoichiometry (orange, circle), normalized against the viscosity with respect to molality.

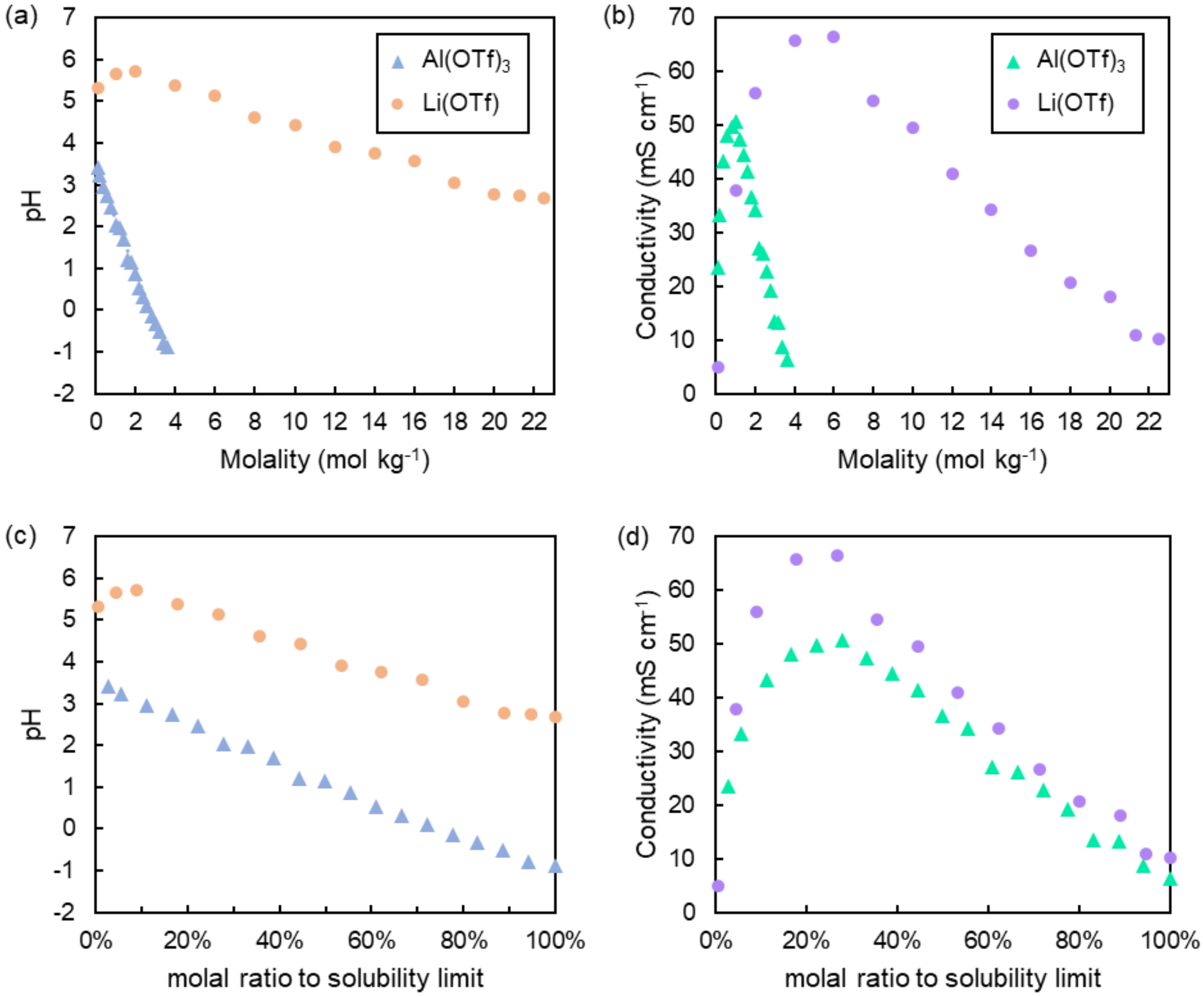

Figure S15. (a, c) pH and (b, d) conductivity of aqueous aluminum and lithium triflate solutions at 20 °C. Both pH and conductivity correspond linearly with concentration as indicated by high R squared values, 0.9925 and 0.9938, respectively.

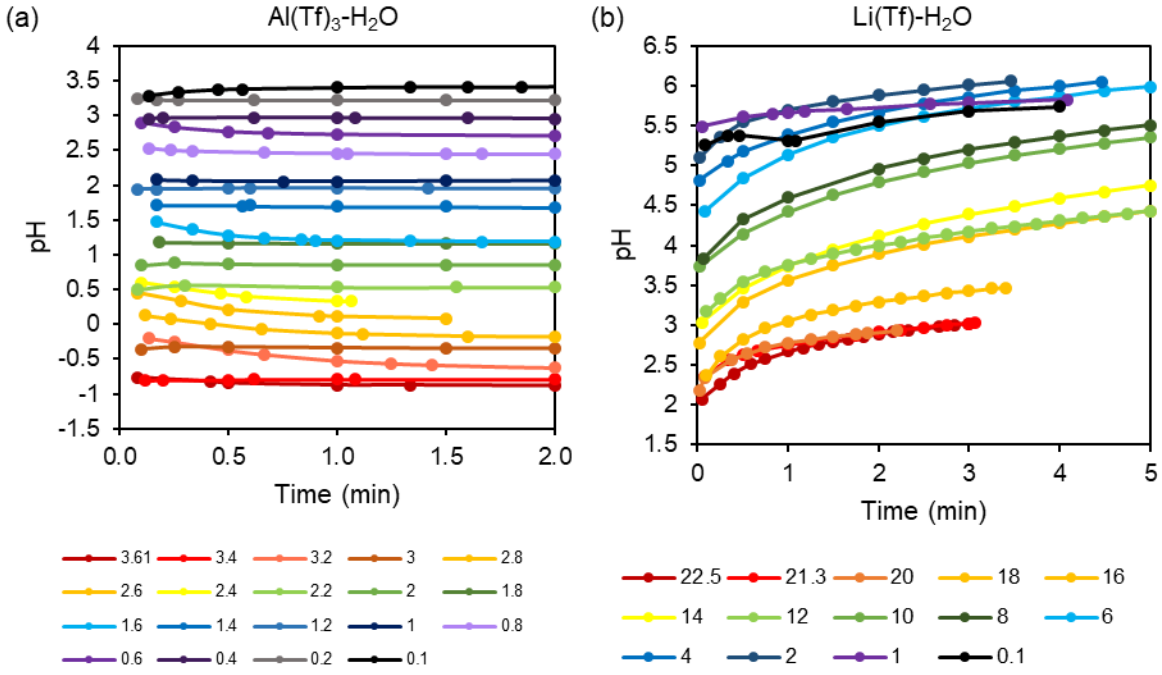

Figure S16. Drift in pH with time for the (a) Al(OTf)$_3$-H$_2$O and (b) Li(OTf)-H$_2$O systems. The latter indicates possible formation of an anion-rich inner Helmholtz layer on the glass electrode. If so, it is worth noting that the true pH of bulk WiSE solutions may be much lower than expected.

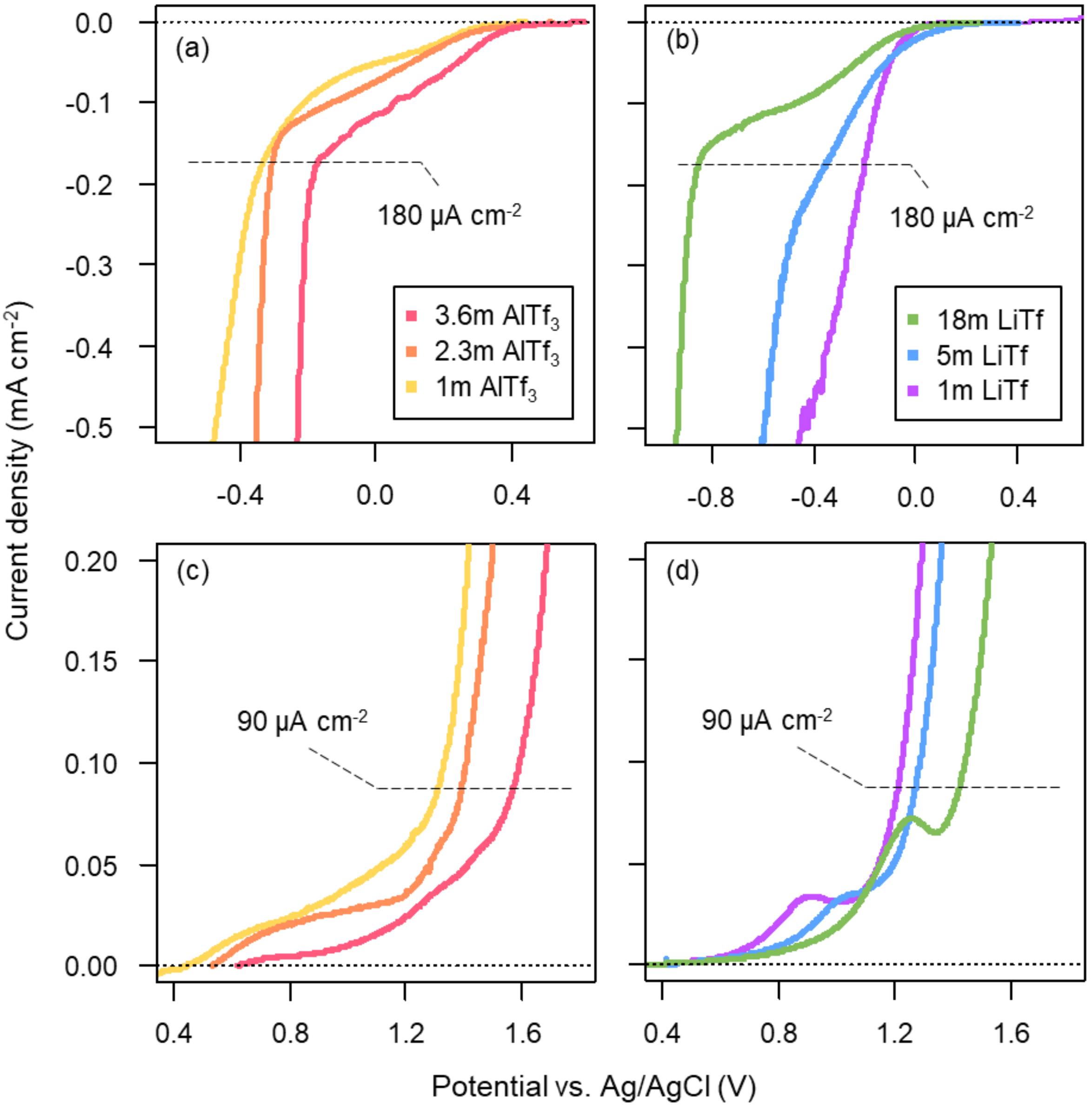

Figure S17. A closer look at the cut-off current density for cathodic and anodic potential sweeps in various aqueous Al and Li triflate solutions from Figure 5. Linear sweep measurements were performed on a Pt working electrode and vitreous carbon counter electrode with a silver/silver chloride reference electrode at 5 mV sec^{-1}.

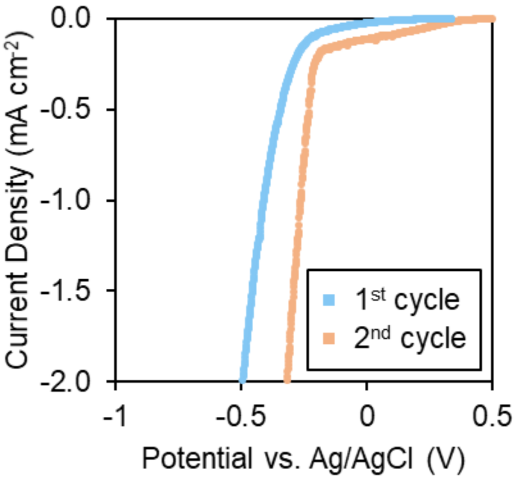

Figure S18. Cathodic sweeps of the 3.6m $Al(OTf)_3$-H_2O solution demonstrate reduced overpotential against HER, likely due to conditioning of the Pt electrode. The formation of a stable SEI could be expected to produce an increase in overpotential, rather than a decrease.

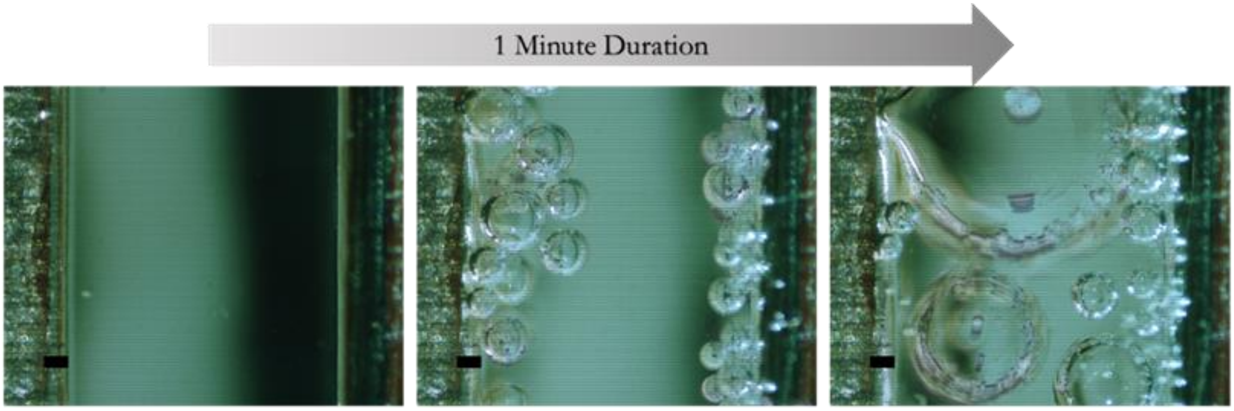

Figure S19. Galvanostatic cycling of an Al|3.6m $Al(OTf)_3$ H_2O|Cu cell, viewed in operando through a glass window of a custom-designed optical configuration. The duration between the first (left) and last image (right) is 1 minute and the current density is 10 mA cm^{-2}.

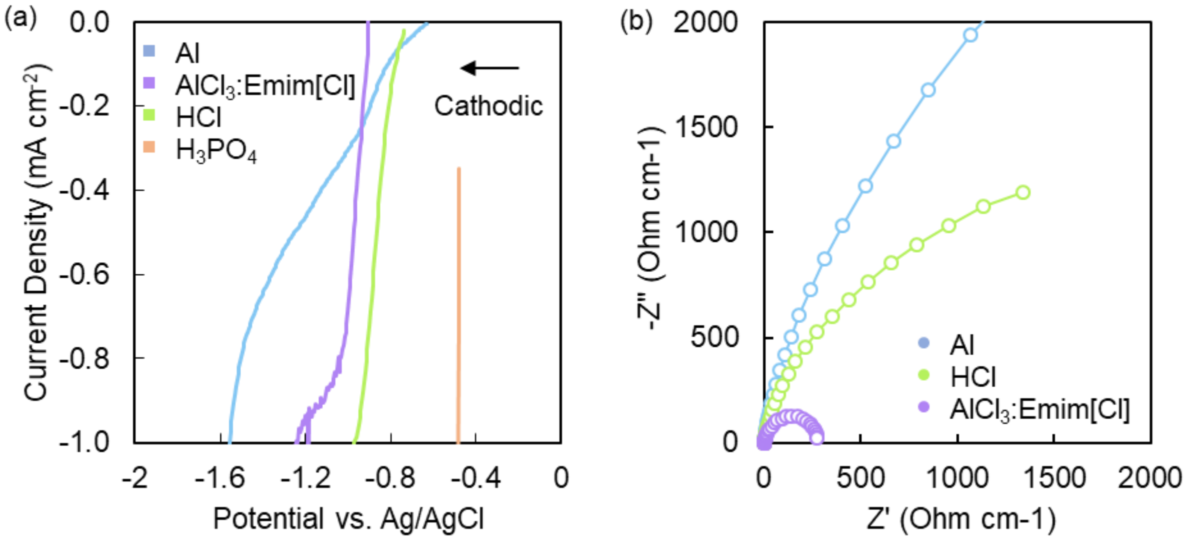

Figure S20. Linear sweep voltammetry and electrochemical impedance spectroscopy of aluminum electrodes with and without pre-treatment, in 1.0 m $Al(OTf)_3$ H_2O electrolyte.

EQUATIONS

Nernst-Einstein relation

$$\sigma_{NE} = (q_+^2 n_+ D_+ + q_-^2 n_- D_-)/k_B T \qquad (1)$$

where q_+, q_-, n_+, n_-, k_B, T, D_+, and D_- represent the valence of the cation, valence of the anion, number of cations, number of anions, Boltzmann constant, temperature, cation diffusivity, and anion diffusivity, respectively. This can be used to approximate the degree of uncorrelated ionic motion (α_d), often called iconicity, which is defined as,

$$\alpha_d = \sigma/\sigma_{NE} \qquad (2)$$

where σ represents the measured conductivity of the solution and σ_{NE} represents the conductivity derived from the Nernst-Einstein equation (1). At high iconicity, an approximation of the transference number for the $Al(OTf)_3$-H_2O system can be defined as,

$$t^{Al^{3+}} = (c_{Al^{3+}} \times D_{Al^{3+}})/(c_{Al^{3+}} \times D_{Al^{3+}} + c_{OTf^-} \times D_{OTf^-} + c_{H^+} \times D_{H^+}) \qquad (3)$$

where $c_{Al^{3+}}$, c_{OTf^-}, and c_{H^+} represent the aluminum, anion, and hydronium concentration, while $D_{Al^{3+}}$, D_{OTf^-}, and D_{H^+} represent aluminum, anion, and hydronium diffusivity, respectively.

TABLES

Table S1. Karl Fisher measurements of 523.7 mg aluminum triflate (SynQuest Laboratories, Inc.) in 1g of dry acetonitrile (24.77 ppm H_2O), before and after various drying methods.

Method	P_4O_{10} (mg)	H_2O (ppm)	Sample (g)	Hydrate (moles)
Wet - 1	0	37,030	0.785	3.18
Wet - 2	0	42,546	0.503	3.72
3Å M.S.	0	30,268	0.741	2.54
100mg P_4O_{10}	100	10,891	0.895	0.90
200mg P_4O_{10}	200	1,873	0.946	0.15
300mg P_4O_{10}	300	401	0.806	0.04

Table S2. Local maxima of the CF_3 bending mode and SO_3 stretching mode in various triflate solutions.

Composition	CF_3	SO_3
0.09 m $AlOTf_3$ H_2O	766	1034
0.9 m $AlOTf_3$ H_2O	766	1034
1.8 m $AlOTf_3$ H_2O	767	1034
3.6 m $AlOTf_3$ H_2O	768	1041
0.1 m LiOTf H_2O	766	1034
1.0 m LiOTf H_2O	766	1034
5.0 m LiOTf H_2O	767	1034
10.0 m LiOTf H_2O	768	1043
0.1 m $ZnOTf_2$ H_2O	766	1034
1.0 m $ZnOTf_2$ H_2O	767	1034
2.0 m $ZnOTf_2$ H_2O	767	1034
4.0 m $ZnOTf_2$ H_2O	768	1037

Table S3. Al^{27}, F^{19} and H^1 diffusion coefficients as measured from a 300 MHz NMR spectrometer at room temperature. * ±10%

$AlOTf_3$ (m)	D_{Al} (m^2/s)	D_F (m^2/s)	D_{H2O} (m^2/s)
0.1	3.96E-10	9.84E-10	2.07E-09
0.5	2.59E-10	6.47E-10	1.40E-09
1.0	1.63E-10	3.89E-10	8.88E-10
2.0	6.90E-11	1.47E-10	3.65E-10
3.0	2.52E-11	5.22E-11	1.86E-10*
3.6	1.56E-11	2.86E-11	8.95E-11*

Table S4. Electrochemical stability window of the aqueous aluminum and lithium triflate electrolytes in 3 electrode beaker cell measurements with Pt working, Ag/AgCl reference, and carbon counter electrodes at 5 mV sec^{-1}.

Composition	Anodic SL (+0.09 mA/cm^{-2})	Cathodic SL (-0.18 mA cm^{-2})	ESW (V)
1.0 m $AlOTf_3$ H_2O	1.44	-0.34	1.78
2.3 m $AlOTf_3$ H_2O	1.53	-0.30	1.82
3.6 m $AlOTf_3$ H_2O	1.58	-0.23	1.94
1.0 m LiOTf H_2O	1.21	-0.20	1.42
5.0 m LiOTf H_2O	1.28	-0.36	1.64
22.5 m LiOTf H_2O	1.43	-0.86	2.29

Table S5. Details of the BOMD simulations performed.

Run	Purpose	Length (ps)	Timestep (fs)	Temp. (K)	Cutoff (Ry)	Thermostat (coupling, fs)
MD - 0	OPLS→DFT	1.0	0.5	50.15	850/60	[a]Mass. CSVR (11.)
MD - 1	Thermalize	2.0	0.5	273.15	850/60	Mass. CSVR (11.)
MD - 2	Thermalize	3.0	0.5	450.15	850/60	Mass. CSVR (11.)
MD - 3	Thermalize	3.0	0.5	600.15	850/60	Mass. CSVR (11.)
MD - 4	Thermalize	3.0	0.5	800.15	850/60	Mass. CSVR (11.)
MD - 5	Equilibration	20.	0.5	800.15	850/60	Mass. CSVR (11.)
MD - 6	Production	30.	0.5	800.15	850/60	Global CSVR (11.)

[a] Massive (coupled to every degree of freedom) velocity rescaling thermostat

Supplementary References

1. D. W. Fong and E. Grunwald, *J. Am. Chem. Soc.*, 1969, **91**, 2413.
2. J. P. Nordin, D. J. Sullivan, B. L. Phillips and W. H. Casey, *Inorganic Chemistry*, 1998, **37**, 4760-4763.
3. M. D. Hanwell, D. E. Curtis, D. C. Lonie, T. Vandermeersch, E. Zurek and G. R. Hutchison, *Journal of Cheminformatics*, 2012, **4**, 17.
4. A. H. Larsen, J. J. Mortensen, J. Blomqvist, I. E. Castelli, R. Christensen, M. Dułak, J. Friis, M. N. Groves, B. Hammer and C. Hargus, *Journal of Physics: Condensed Matter*, 2017, **29**, 273002.
5. M. J. Frisch, G. W. Trucks, H. B. Schlegel, G. E. Scuseria, M. A. Robb, J. R. Cheeseman, G. Scalmani, V. Barone, G. A. Petersson, H. Nakatsuji, X. Li, M. Caricato, A. V. Marenich, J. Bloino, B. G. Janesko, R. Gomperts, B. Mennucci, H. P. Hratchian, J. V. Ortiz, A. F. Izmaylov, J. L. Sonnenberg, Williams, F. Ding, F. Lipparini, F. Egidi, J. Goings, B. Peng, A. Petrone, T. Henderson, D. Ranasinghe, V. G. Zakrzewski, J. Gao, N. Rega, G. Zheng, W. Liang, M. Hada, M. Ehara, K. Toyota, R. Fukuda, J. Hasegawa, M. Ishida, T. Nakajima, Y. Honda, O. Kitao, H. Nakai, T. Vreven, K. Throssell, J. A. Montgomery Jr., J. E. Peralta, F. Ogliaro, M. J. Bearpark, J. J. Heyd, E. N. Brothers, K. N. Kudin, V. N. Staroverov, T. A. Keith, R. Kobayashi, J. Normand, K. Raghavachari, A. P. Rendell, J. C. Burant, S. S. Iyengar, J. Tomasi, M. Cossi, J. M. Millam, M. Klene, C. Adamo, R. Cammi, J. W. Ochterski, R. L. Martin, K. Morokuma, O. Farkas, J. B. Foresman and D. J. Fox, *Journal*, 2016.
6. L. Cao, D. Li, T. Pollard, T. Deng, B. Zhang, C. Yang, L. Chen, J. Vatamanu, E. Hu, M. J. Hourwitz, L. Ma, M. Ding, Q. Li, S. Hou, K. Gaskell, J. T. Fourkas, X.-Q. Yang, K. Xu, O. Borodin and C. Wang, *Nature Nanotechnology*, 2021, DOI: 10.1038/s41565-021-00905-4.
7. I. M. Alecu, J. Zheng, Y. Zhao and D. G. Truhlar, *Journal of Chemical Theory and Computation*, 2010, **6**, 2872-2887.
8. L. Martínez, R. Andrade, E. G. Birgin and J. M. Martínez, *J Comp Chem*, 2009, **30**.
9. H. J. Berendsen, J. P. Postma, W. F. van Gunsteren and J. Hermans, in *Intermolecular Forces*, Springer, 1981, pp. 331-342.
10. B. Doherty, X. Zhong, S. Gathiaka, B. Li and O. Acevedo, *Journal of Chemical Theory and Computation*, 2017, **13**, 6131-6145.
11. T. M. C. Faro, G. P. Thim and M. S. Skaf, *The Journal of Chemical Physics*, 2010, **132**, 114509.
12. J. W. Ponder, *Washington University School of Medicine, Saint Louis, MO*, 2004, **3**.
13. G. Bussi, D. Donadio and M. Parrinello, *The Journal of Chemical Physics*, 2007, **126**, 014101.
14. H. J. Berendsen, J. v. Postma, W. F. van Gunsteren, A. DiNola and J. Haak, *The Journal of Chemical Physics*, 1984, **81**, 3684-3690.
15. J. Hutter, M. Iannuzzi, F. Schiffmann and J. VandeVondele, *Wiley Interdisciplinary Reviews-Computational Molecular Science*, 2014, **4**, 15-25.
16. Y. Zhang and W. Yang, *Physical Review Letters*, 1998, **80**, 890-890.
17. S. Grimme, S. Ehrlich and L. Goerigk, *Journal of Computational Chemistry*, 2011, **32**, 1456-1465.
18. S. Grimme, J. Antony, S. Ehrlich and H. Krieg, *Journal of Chemical Physics*, 2010, **132**, 154104.
19. J. VandeVondele and J. Hutter, *Journal of Chemical Physics*, 2007, **127**, 114105.
20. J. VandeVondele, M. Krack, F. Mohamed, M. Parrinello, T. Chassaing and J. Hutter, *Comput. Phys. Commun.*, 2005, **167**, 103.
21. J. VandeVondele and J. Hutter, *J. Chem. Phys.*, 2003, **118**, 4365.
22. C. Hartwigsen, S. Goedecker and J. Hutter, *Physical Review B*, 1998, **58**, 3641-3662.
23. S. Goedecker, M. Teter and J. Hutter, *Physical Review B Condens Matter*, 1996, **54**, 1703-1710.
24. R. Hanson, *Journal of Applied Crystallography*, 2010, **43**, 1250-1260.
25. M. Brehm and B. Kirchner, *Journal of Chemical Information and Modeling*, 2011, **51**, 2007-2023.